

Electronic Supplementary Information

The CoWO₄ Nanoparticles with Dual Active Sites for Highly Efficient Ammonia Synthesis

Lian Duan,^{†a} Zhencong Huang,^{†a} Gen Chen,^a Min Liu,^b Xiaohe Liu,^c Renzhi Ma^{*d} and Ning Zhang^{*a}

^a School of Materials Science and Engineering, Central South University, Changsha 410083, China

* Email: nzhang@csu.edu.cn

^b School of Physics and Electronics, Central South University, Changsha 410083, China

^c School of Chemical Engineering, Zhengzhou University, Zhengzhou 450001, China

^d Research Center for Materials Nanoarchitectonics (MANA), National Institute for Materials Science (NIMS), Tsukuba, Ibaraki 305-0044, Japan

* Email: ma.renzhi@nims.go.jp

[†] These authors contribute equally to this work.

Table of Contents

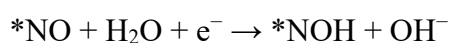
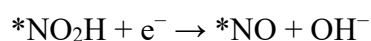
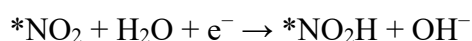
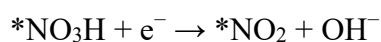
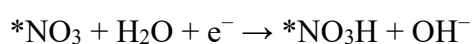
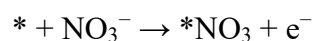
1. Supplementary Experimental Section
2. Supplementary Figures
3. Supplementary Tables

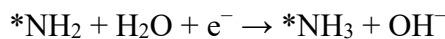
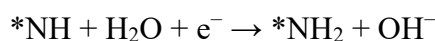
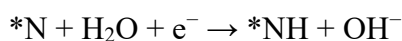
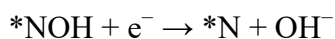
Supplementary Experimental Section

DFT calculations. In this study, all theoretical calculations were carried out by the Vienna ab-initio Simulation Package (VASP) based on the density functional theory (DFT).¹ The generalized gradient approximation (GGA) in the form of Perdew-Burke-Ernzerhof (PBE) exchange-correlation functional was used to describe the electron exchange-correlation.² The interaction between electron and ion was treated by the projector augmented wave (PAW) method.³ Grimme's DFT-D3 method was incorporated to implement the van der Waals correction.⁴ The cut-off energy of 500 eV was set for all calculations. For all calculations, the final force on each atom was less than 0.05 eV/Å for each ionic step, and the convergence criterion for the self-consistent field energy was set to be 1.0×10^{-5} eV. A 2×2 supercell of WO₃ (001) surface, CoWO₄ (001) surface and Co₃O₄ (001) surface was used as the models for WO₃, CoWO₄ and Co₃O₄ catalyst, respectively. For all models, the vacuum thickness was set to be 20 Å to minimize interlayer interactions. A Monkhorst–Pack k-point mesh of $3 \times 3 \times 1$ was used for structural Optimizations. The Gibbs reaction free energy (ΔG) was calculated based on the computational hydrogen electrode (CHE) model.⁵ In this study, N-end pathway was considered as the most favorable pathway on catalysts surface, which involves the intermediates *NO₃, *NO₃H, *NO₂, *NO₂H, *NO, *NOH, *N, *NH, *NH₂ and *NH₃.⁶ The whole reaction for electrochemical reduction of NO₃⁻ to NH₃ can be summarized as:



The elementary steps of N-end pathway can be described as:





Here, (*) represent the adsorption site. The Gibbs free energy change (ΔG) of each elementary reaction was calculated as follows:

$$\Delta G = \Delta E + \Delta ZPE - T \times \Delta S$$

where ΔE is the difference of electronic energy between products and reactants, ΔZPE is the change of zero-point energies, and ΔS is the entropy change.

Chemicals. Cobalt nitrate hexahydrate ($\text{Co}(\text{NO}_3)_2 \cdot 6\text{H}_2\text{O}$, AR, 99%), Sodium carbonate (Na_2CO_3 , 99.9%) ammonium chloride (NH_4Cl , AR, 99.5%), Potassium nitrite (KNO_2 , AR, 97%), sulfanilamide ($\text{C}_6\text{H}_8\text{N}_2\text{O}_2\text{S}$, AR, $\geq 99\%$), N-(1-naphthyl) ethylenediamine dihydrochloride ($\text{C}_{12}\text{H}_{14}\text{N}_2 \cdot 2\text{HCl}$, AR, 98%) were purchased from Aladdin Bio-Chem Technology Co., Ltd. Sodium tungstate dihydrate ($\text{Na}_2\text{WO}_4 \cdot 2\text{H}_2\text{O}$, AR), sodium nitrate (NaNO_3 , AR, $\geq 99\%$), hydrochloric acid (HCl , GR, 38%) and Sodium hydroxide (NaOH , AR, $\geq 96\%$) were purchased from Sinopharm Chemical Reagent Co., Ltd. Sodium salicylate ($\text{C}_7\text{H}_5\text{NaO}_3$, AR, 99.5%), Potassium sodium tartrate tetrahydrate ($\text{C}_4\text{H}_4\text{O}_6\text{KNa} \cdot 4\text{H}_2\text{O}$), Sodium nitroferricyanide (III) dihydrate ($\text{C}_5\text{FeN}_6\text{Na}_2\text{O} \cdot 2\text{H}_2\text{O}$, metals basis, 99.98%) were purchased from McLean Biochemical Technology Co., Ltd. All chemicals were used without further purification. Conductive carbon paper was purchased from Cyber Electrochemical Materials Network. Deionized water (DI, 18.2 M Ω) was used in the overall process of catalysts preparation and performance test.

Material characterizations. XRD patterns were obtained using a RIGAKU Rint-2000 X-ray diffractometer with Cu K α radiation ($\lambda = 1.54184 \text{ \AA}$). The scanning 2θ range is 5-80 $^\circ$ with a

scan rate of 4 °/min. SEM images were collected by using a JSM-7610FPlus (JEOL, Japan) field emission scanning electron microscopy. TEM, HRTEM, SAED patterns and elemental mapping were carried out on a FEI Tecnai G2 F20 field emission transmission electron microscope (equipped with an EDX integrated) with an operating voltage of 200 kV. XPS was recorded using a Thermo Scientific K-Alpha spectrophotometer equipped with a monochromatic Al K α X-ray source (1487 eV). The binding energy of all XPS spectra was calibrated based on the C1s characteristic at 284.8 eV. The X-ray absorption spectroscopy of W L-edge was measured at the BL14W1 beamline in the Shanghai Synchrotron Radiation. All XAS data analyses were performed with the Athena software package to extract XANES. The colorimetric method on a UV-vis spectrophotometer (UV-2600) was used to quantify the produced ammonia. In-situ electrochemical ATR-FTIR measurements were performed by using Thermo iS50.

Electrochemical measurements. In this work, all electrochemical measurements were conducted on a CHI 760e electrochemical workstation at room temperature. The electrolysis system comprised a conventional three-electrode hydrogen ion cell and a proton exchange membrane (Nafion 117). The working electrode, counter electrode, and reference electrode were prepared using carbon paper loaded with catalysts, platinum foil, and Hg/HgO filled with 1 M KOH solution, respectively. The working electrode was prepared by dispersing 10 mg of the prepared catalyst in a mixed solution of 2 mL of distilled water (1 mL), ethanol (1 mL), and 5 wt.% Nafion (25 μ L), and then subjecting it to ultrasonication for a period exceeding 60 minutes in order to obtain a uniform ink. Subsequently, 50 μ L of the aforementioned ink was deposited onto a 0.25 cm² area of carbon paper.

LSV curves was used to preliminarily evaluate the NO₃RR activity of the material at a scan rate of 10 mV s⁻¹, with the potential range set at -0.6 to -1.9 V (vs Hg/HgO). Before the LSV test, the working electrode was subjected to 100 CV tests in the potential range of -0.7V to -1.1 V

(vs Hg/HgO) to stabilize the material activation, with a scan rate of 50 mV s^{-1} . In order to determine the ECSA of different samples, a series of CV curves with different scan rates (20, 40, 60, 80, 100, 120 and 140 mV s^{-1}) were tested in the non-Faraday potential range of 0.75 V to 0.85 V (vs RHE), and the ECSA of the samples was obtained by fitting. The samples were tested by EIS at a potential of -1.2 V (vs Hg/HgO) with a frequency range of 0.1 Hz to 100 kHz. The electrochemical test was carried out in 1 M NaOH + 0.1 M NaNO₃ electrolyte. In order to evaluate the FE of the catalyst NO₃RR to synthesize NH₃, the catalyst was subjected to constant potential electrolysis test for 30 min at different potentials (-0.2 , -0.3 , -0.4 , -0.5 , -0.6 and -0.7 V vs RHE). After the reaction, the cathode electrolyte was collected and diluted to a suitable concentration for color development. Subsequently, the UV-visible absorbance UV curve of the solution was measured to calculate the FE and NH₃ yield of the sample. The voltage (vs Hg/HgO) of all electrochemical tests was converted to the voltage relative to RHE using the following equation: $E \text{ (vs RHE)} = E \text{ (vs Hg/HgO)} + 0.098 \text{ V} + 0.059 \times \text{pH}$.

NH₃ quantification. The quantity of NH₃ produced was determined using the indophenol blue method. In the typical procedure, a certain quantity of electrolyte was initially extracted from the cathodic reaction cell and diluted to a volume of 2 mL. Subsequently, 2 mL of a 1 M NaOH solution containing 5 wt.% salicylic acid and 5 wt.% sodium citrate, and 1 mL of a freshly prepared 0.05 M NaClO solution were added. The solution was then agitated for a few seconds. Subsequently, 0.2 mL of a 1 wt.% sodium nitroferricyanide solution was added to the catholyte and allowed to react for one hour at room temperature. Subsequently, the absorbance curves of the catholyte were recorded using an ultraviolet–visible (UV–Vis) spectrophotometer in the wavelength range of 400–800 nm. The concentration of ammonia was determined by measuring the absorbance at approximately 655 nm. In order to quantify the amount of NH₃, a calibration curve was plotted for the determination of NH₃, with the concentrations of standard NH₄Cl solutions (0, 2, 4, 6, 8 and $10.0 \mu\text{g mL}^{-1}$) plotted against their respective absorbance values.

Nessler's reagent method. To calibrate the concentration-absorbance curve, 2 mL standard ammonia chloride solution with the concentrations of 0, 0.2, 0.4, 0.6, 0.8, 1.0, 1.2, 1.6 and 2.0 $\mu\text{g mL}^{-1}$ were mixed with 0.1 mL of potassium sodium tartrate solution (0.5 g mL^{-1}) and 0.1 mL of Nessler's reagent solution, respectively. After 30 min, the above solution was drawn out for UV-vis absorbance measurement at 420 nm. We then plotted the profile of absorbance value vs the concentrations of standard solution by thrice independent calibrations, where a linear correlation with $R^2 = 0.999$ was obtained. To quantify the generated NH_3 during electrocatalysis, 0.1 mL of potassium sodium tartrate solution (0.5 g mL^{-1}) and 0.1 mL of Nessler's reagent solution were added into 2 mL of the reaction solution. After 30 min, the above solution was drawn out for UV-vis absorbance measurement at 420 nm. According to the light absorbance and standard curve, the ammonia concentration was obtained.

NO_2^- quantification. The concentration of NO_2^- was determined by the method of N-(1-naphthyl) ethylenediamine dihydrochloride with a UV-Vis spectrophotometer. Firstly, the sulfanilamide solution (reagent A) was prepared by dissolving 0.50 g of sulfanilamide in 50.0 mL of a 2.0 M HCl solution. Subsequently, 20.0 mg of N-(1-naphthyl) ethylenediamine dihydrochloride was dissolved in 20.0 mL of deionized water to obtain Reagent B. In a typical experimental setup for NO_2^- determination, 3.0 mL of standard solutions or samples (prepared by diluting with 2 M HCl to form a neutral electrolyte) was added to a sample bottle (5 mL), followed by the addition of 0.06 mL of Reagents A and B, respectively. Following a 30-minute period of aging under ambient conditions, the absorbance curve of the mixed solution was recorded by UV-Vis spectrophotometer in the wavelength range of 450–650 nm. A calibration curve for the determination of NO_2^- was constructed by fitting the NO_2^- concentrations of standard KNO_2 solutions (0, 2.5, 5, 10, 20, and 40 μM) versus their respective absorbance values.

Calculation of the FE_{NH_3} , Y_{NH_3} and $FE_{NO_2^-}$. The FE was defined as the charge consumed for the formation of a specific product divided by the total charge passing through the electrodes (Q) during electrolysis. Given that eight electrons are consumed to produce one NH_3 molecule, the FE_{NH_3} , Y_{NH_3} can be calculated as follows:

$$FE_{NH_3} = (8 \times F \times C_{NH_3} \times V) / Q \quad (Q = I \times t),$$

$$Y_{NH_3} = (C_{NH_3} \times V) / (S \times t).$$

where C_{NH_3} is the concentration of NH_3 in catholyte after reduction, $mol\ mL^{-1}$; V is the volume of catholyte, mL; F is the Faradaic constant, $96485\ C\ mol^{-1}$; I is the total current, A; t is the electrolysis time, s; S is the active area of electrode, cm^2 .

Given that two electrons are consumed to produce one NO_2^- molecule, the FE of NO_2^- ($FE_{NO_2^-}$) can be calculated as follows:

$$FE_{NO_2^-} = (2 \times F \times C_{NO_2^-} \times V) / Q \quad (Q = I \times t)$$

where $C_{NO_2^-}$ is the concentration of NO_2^- in catholyte after reduction, $mol\ mL^{-1}$.

In situ ATR-FTIR spectroscopy. In situ attenuated total reflection Fourier transformed infrared spectroscopy (ATR-FTIR) was obtained on a Thermoelectric IR spectrometer (Thermo Fisher IS50) equipped with a liquid N_2 -cooled MCT-A detector. A thin gold film was deposited on the surface of a silicon crystal via a chemical deposition process. The sample was prepared by depositing the ink on the aforementioned gold film supported by silicon, which was then used as the working electrode. The counter electrode was composed of platinum foil, while the reference electrode was comprised of Ag/AgCl. The electrolyte was a solution of 1M NaOH and 0.1M $NaNO_3$. The FTIR spectra were obtained from an average of 32 scans with a resolution of $8\ cm^{-1}$. The background spectrum was obtained at the open-circuit potential. The spectra dependent on potential were obtained by applying single potential steps and were collected after running 30s.

Supplementary Figures

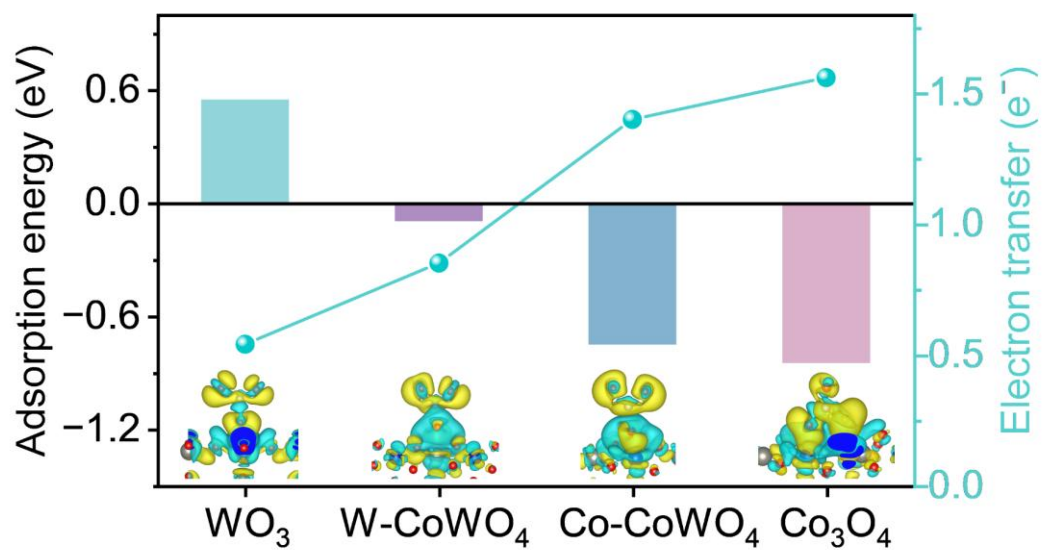


Figure S1 The electron transfer and adsorption energies of $*NO_3$ on WO_3 , W sites of $CoWO_4$, Co sites of $CoWO_4$ and Co_3O_4 (Insets are the charge density differences of $*NO_3$ adsorbed on catalysts surface).

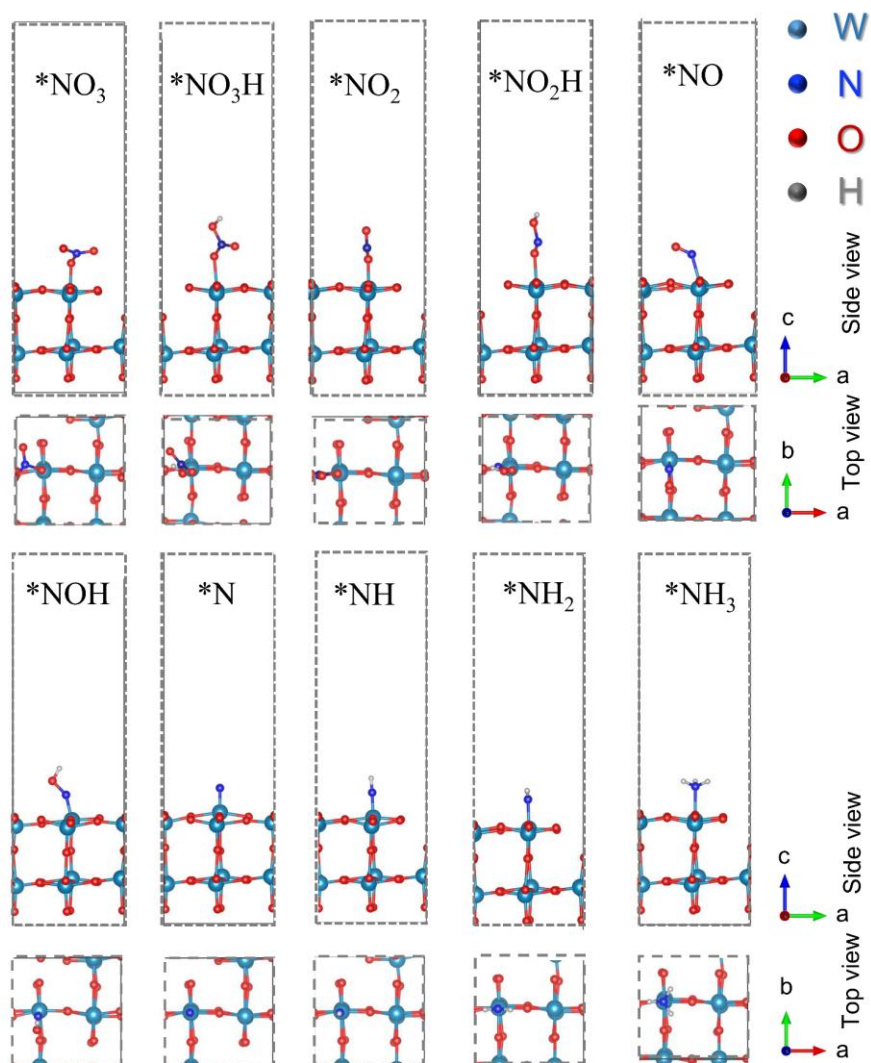


Figure S2 Adsorption configurations of reaction intermediates on (001) surface of WO_3 .

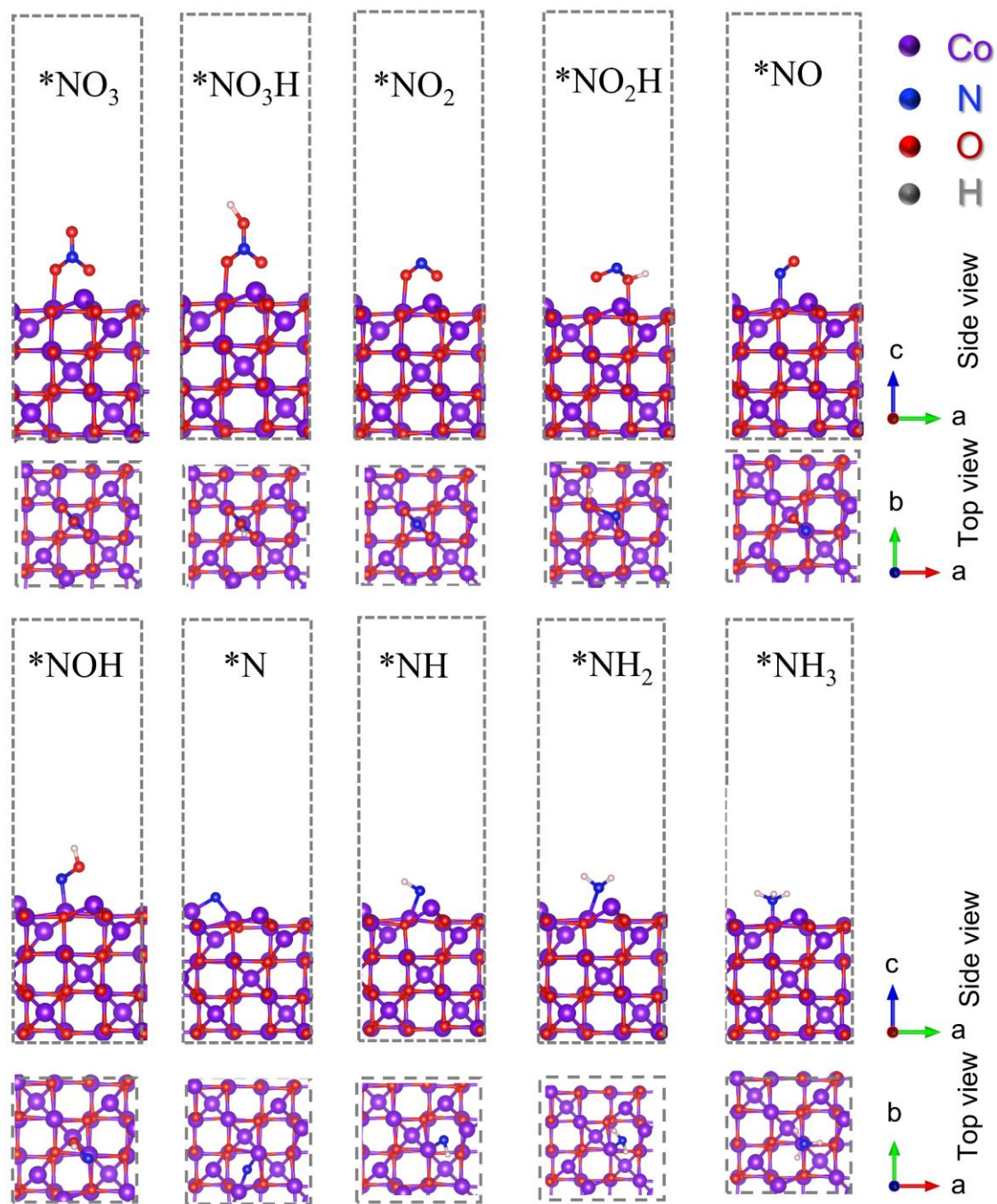


Figure S3 Adsorption configurations of reaction intermediates on (001) surface of Co_3O_4 .

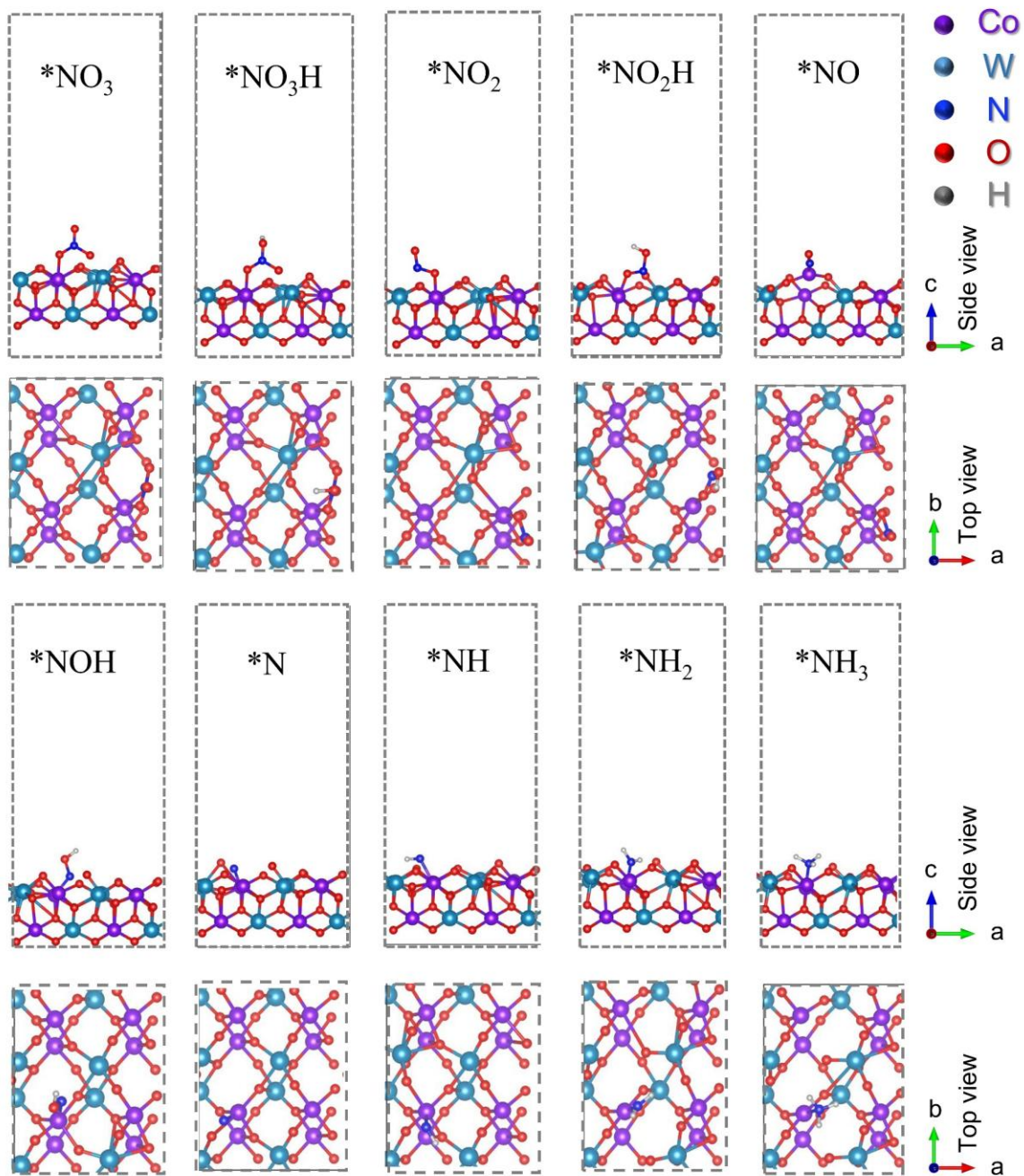


Figure S4 Adsorption configurations of reaction intermediates on (001) surface of CoWO_4 .

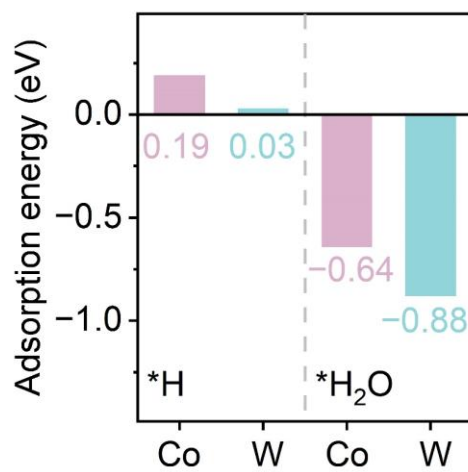


Figure S5 Adsorption energies of *H and *H₂O on Co and W sites in CoWO₄.

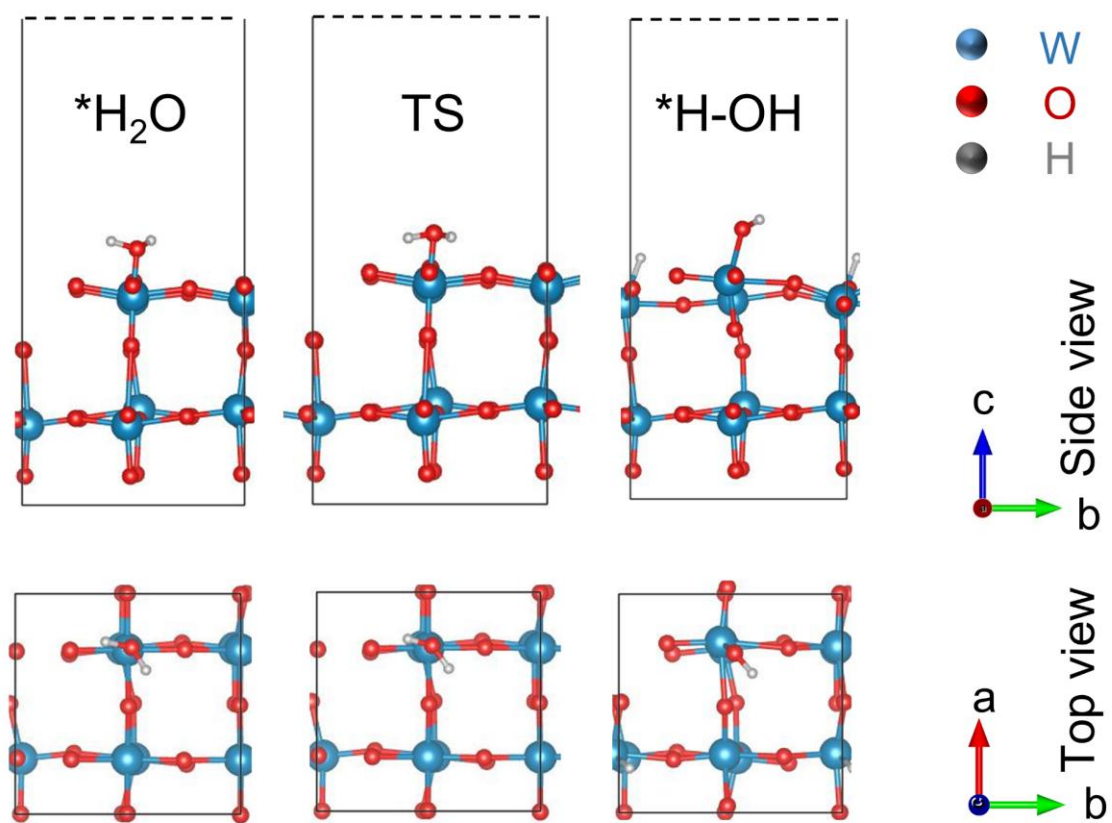


Figure S6 H₂O dissociation process on the surface of WO₃. TS is transient states.

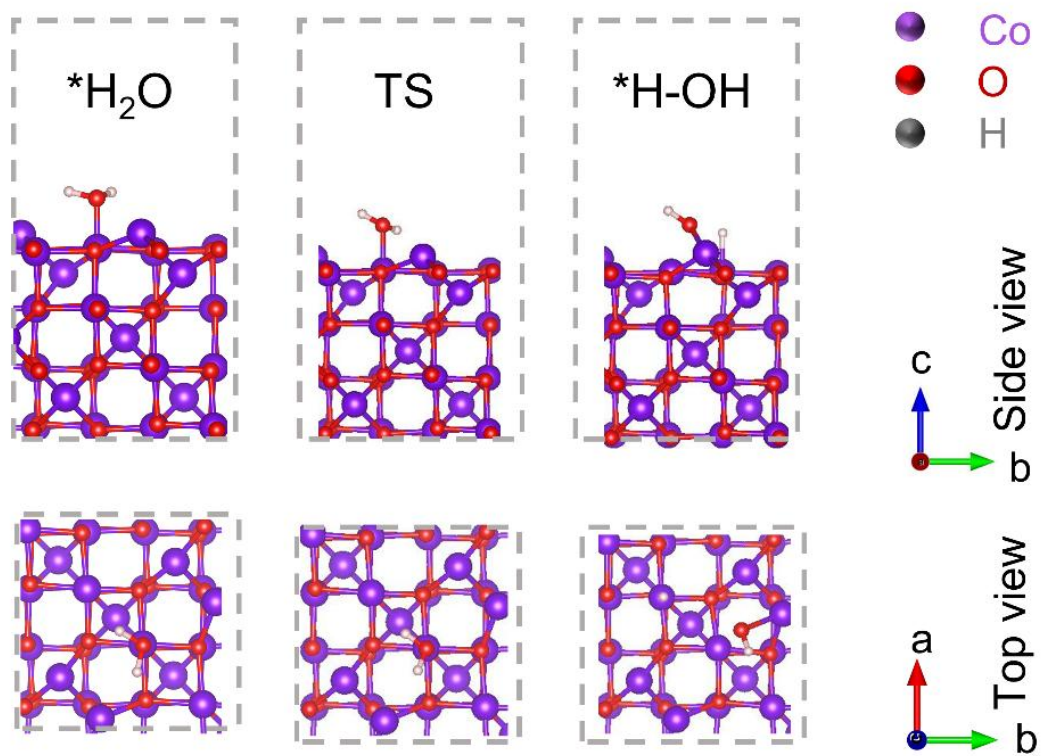


Figure S7 H_2O dissociation process on the surface of Co_3O_4 . TS is transient states.

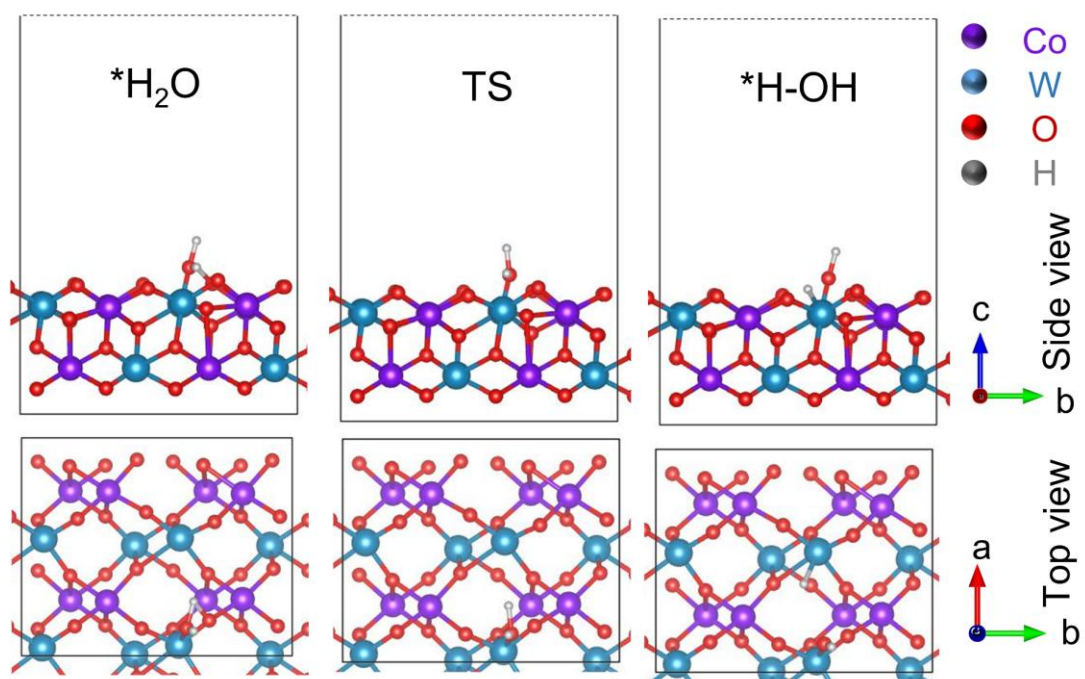


Figure S8 H₂O dissociation process on the surface of CoWO₄. TS is transient states.

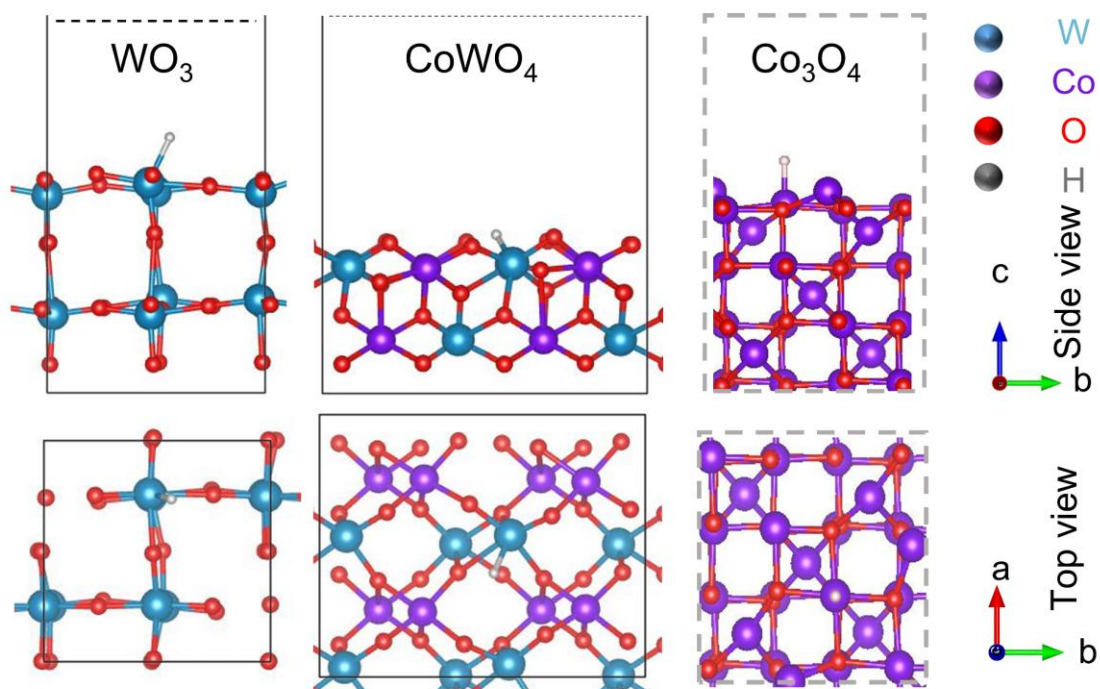


Figure S9 Hydrogen evolution reaction on the (001) surface of WO_3 , CoWO_4 , and Co_3O_4 : The adsorption configurations of $*\text{H}$.

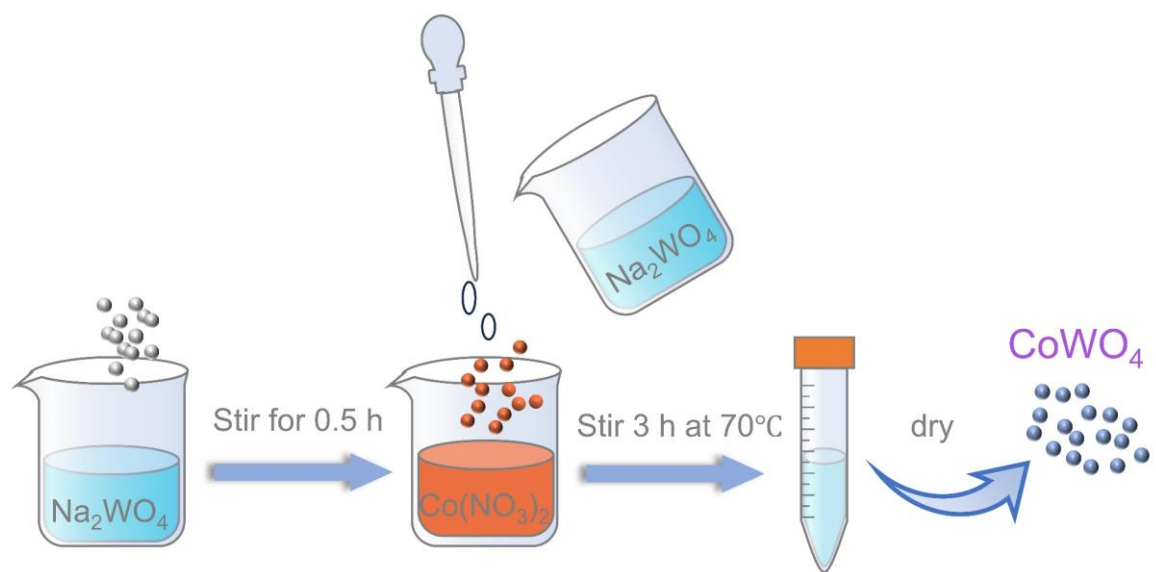


Figure S10 Schematic diagram of the preparation process of CoWO_4 nanoparticles.

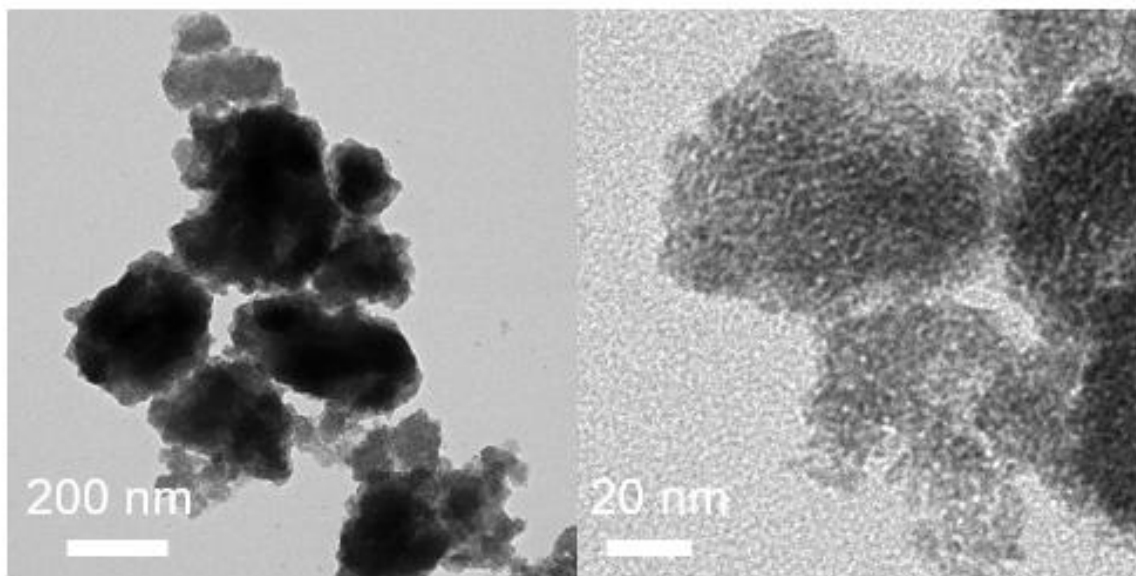


Figure S11 TEM images of CoWO₄.

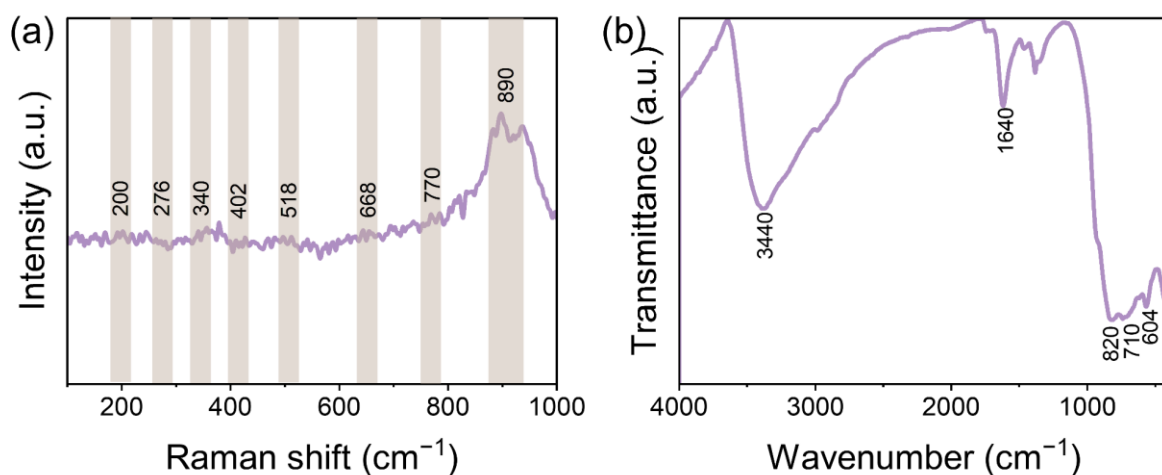


Figure S12 (a) Raman spectra and (b) FT-IR spectra of CoWO_4 .

As illustrated in **Fig. S12a**, the Raman spectrum of CoWO_4 features a sharp peak at 880 cm^{-1} and a weak band at 770 cm^{-1} , which are attributed to the symmetric and asymmetric stretching vibrations of terminal $\text{W}^{1/4}\text{O}$ bonds, respectively. The asymmetric stretching of O-W-O generates the weak bands at 668 and 518 cm^{-1} . The peaks observed at 340 and 402 cm^{-1} are attributed to in-plane rotation and deformation of W-O bonds, respectively. The weak band at 276 cm^{-1} is attributed to Co-O stretching.⁷⁻⁹ **Fig. S12b** illustrates the FT-IR of CoWO_4 . At 3440 and 1640 cm^{-1} belonging to the -OH stretching and bending vibrations of adsorbed water, while at 820 , 710 , and 604 cm^{-1} can be attributed to the vibrational deformation of W-O-W, W-O, and Co-O.^{9, 10}

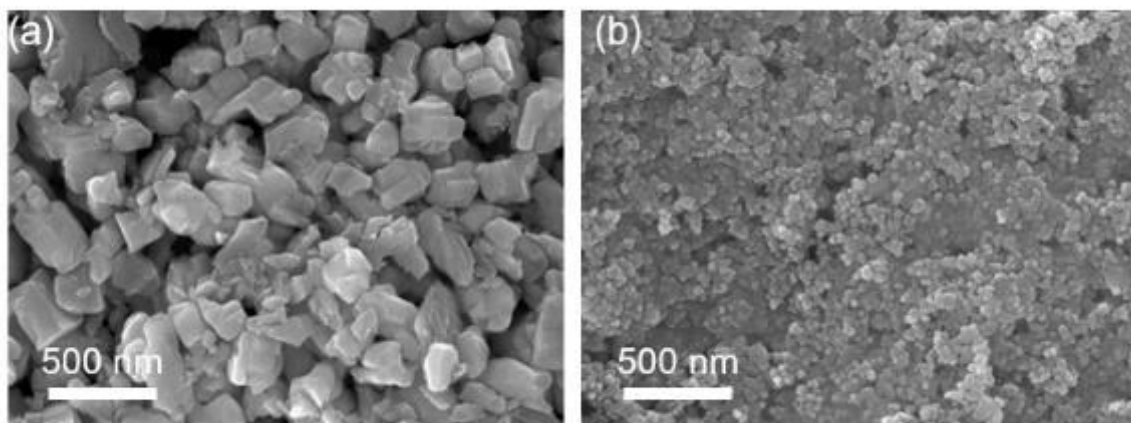


Figure S13 SEM images of (a) WO_3 , (b) Co_3O_4 .

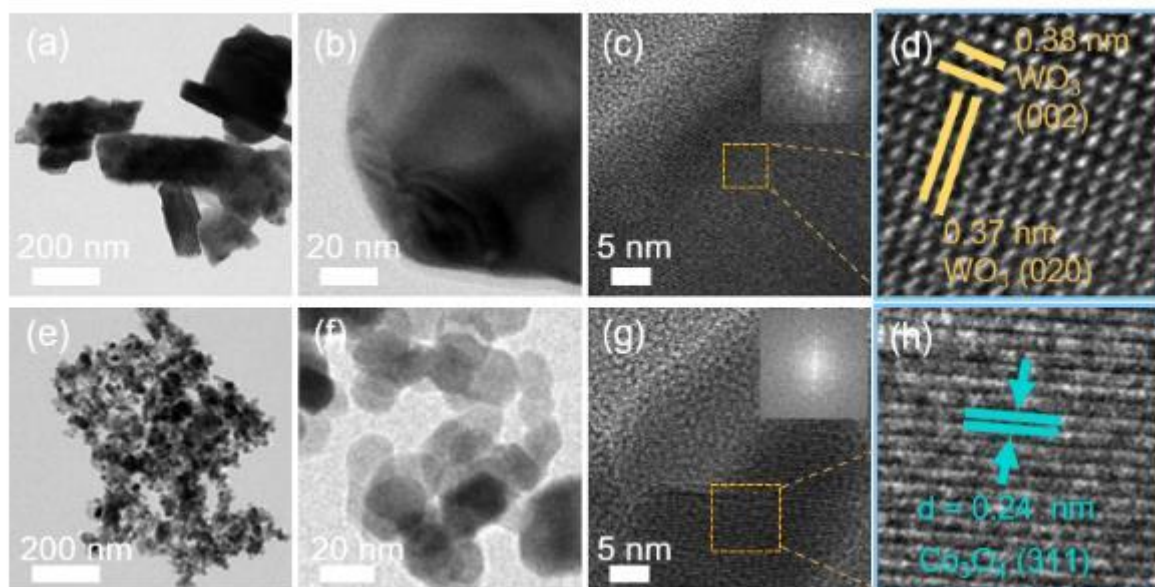


Figure S14 (a, b) TEM, (c) HR-TEM and (d) enlarged HR-TEM of WO₃; (e, f) TEM, (g) HR-TEM and (h) enlarged HR-TEM of Co₃O₄.

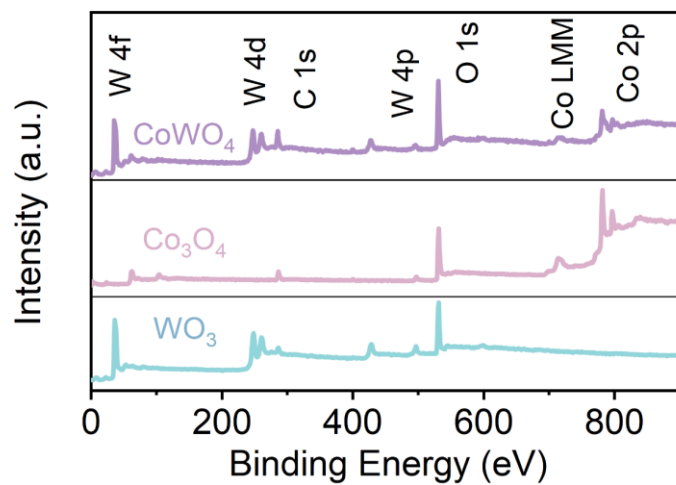


Figure S15 XPS survey spectrum of CoWO₄, WO₃ and Co₃O₄.

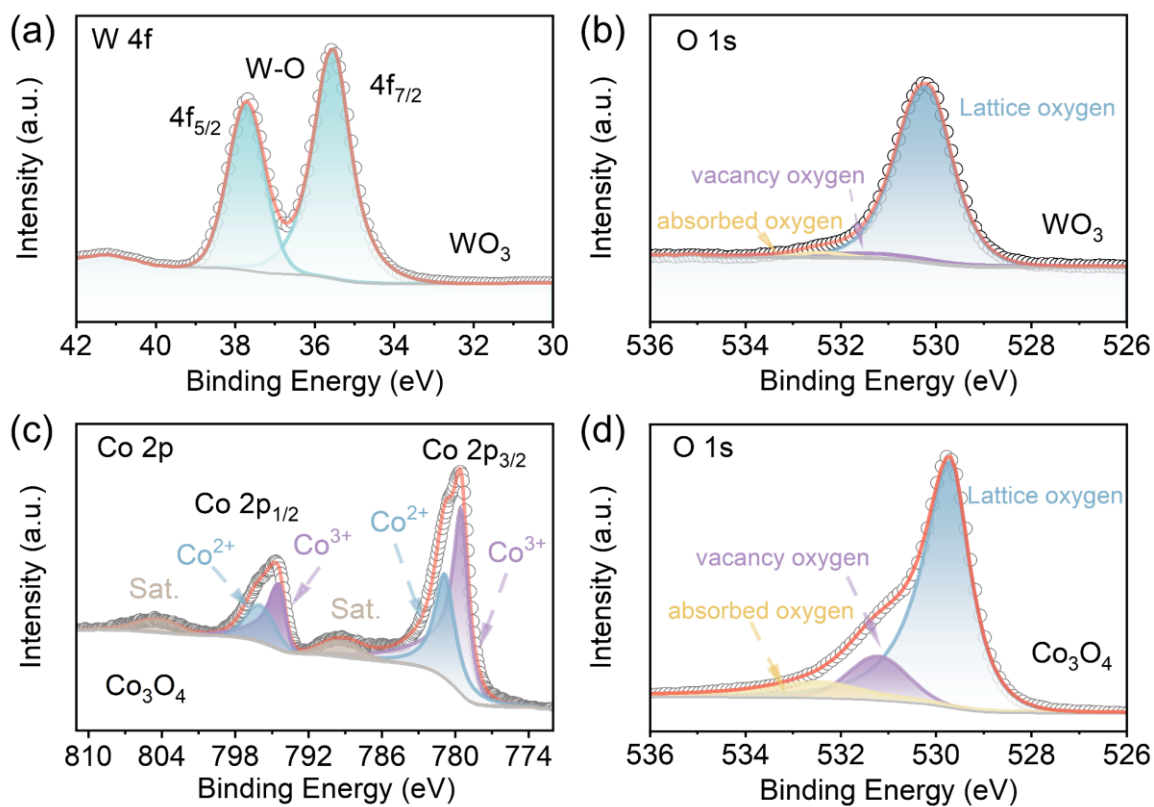


Figure S16 High resolution XPS spectra of (a) W 4f and (b) O 1s for WO_3 ; high resolution XPS spectra of (c) Co 2p and (d) O 1s for Co_3O_4 .

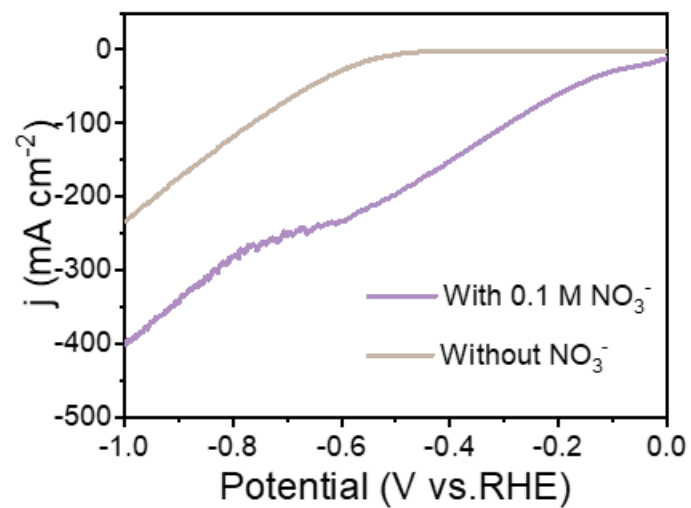


Figure S17 The LSV curves of CoWO₄ measured in 1M NaOH electrolyte with the presence and absence of NO₃⁻.

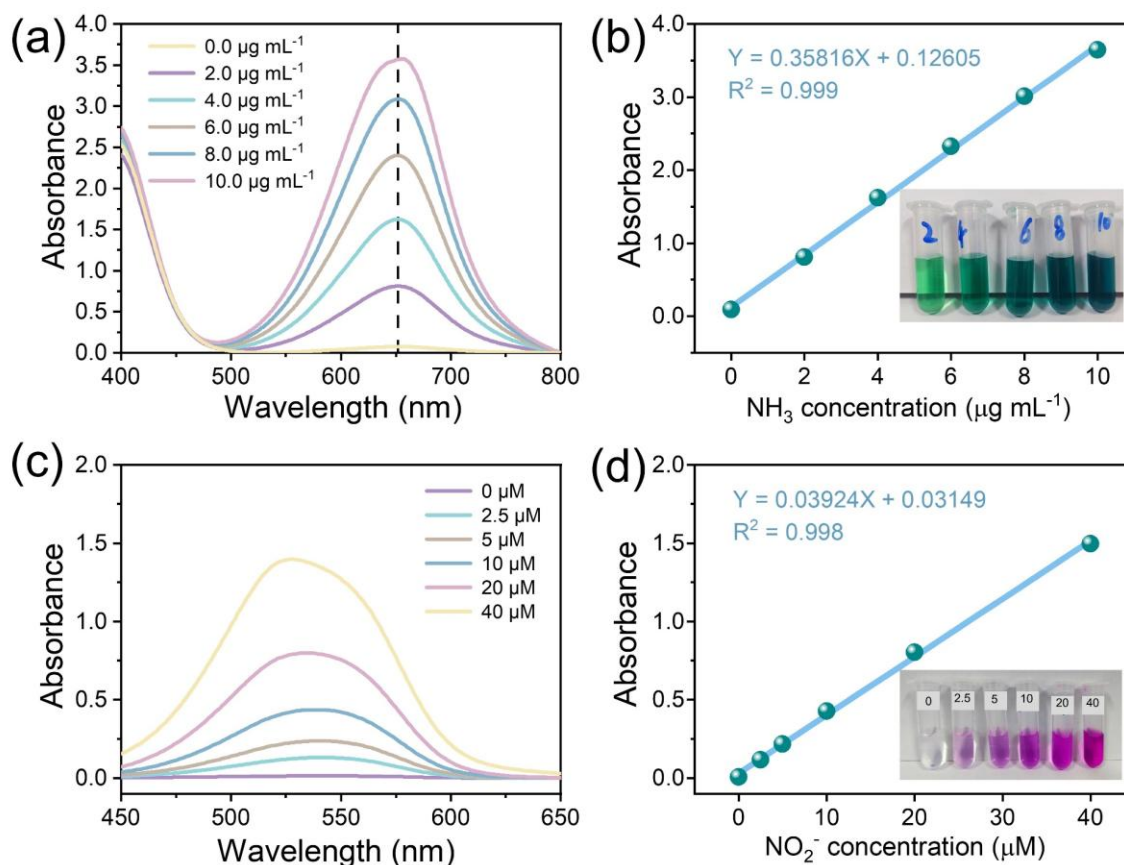


Figure S18 The quantification of NH_3 and NO_2^- . (a) UV-vis absorption spectra for the standard NH_3 solutions with different concentrations; (b) corresponding calibration curve for the NH_3 assay by using the indophenol blue method; (c) UV-vis absorption spectra for the standard NO_2^- solutions with different concentrations and (d) corresponding calibration curve for the NO_2^- assay.

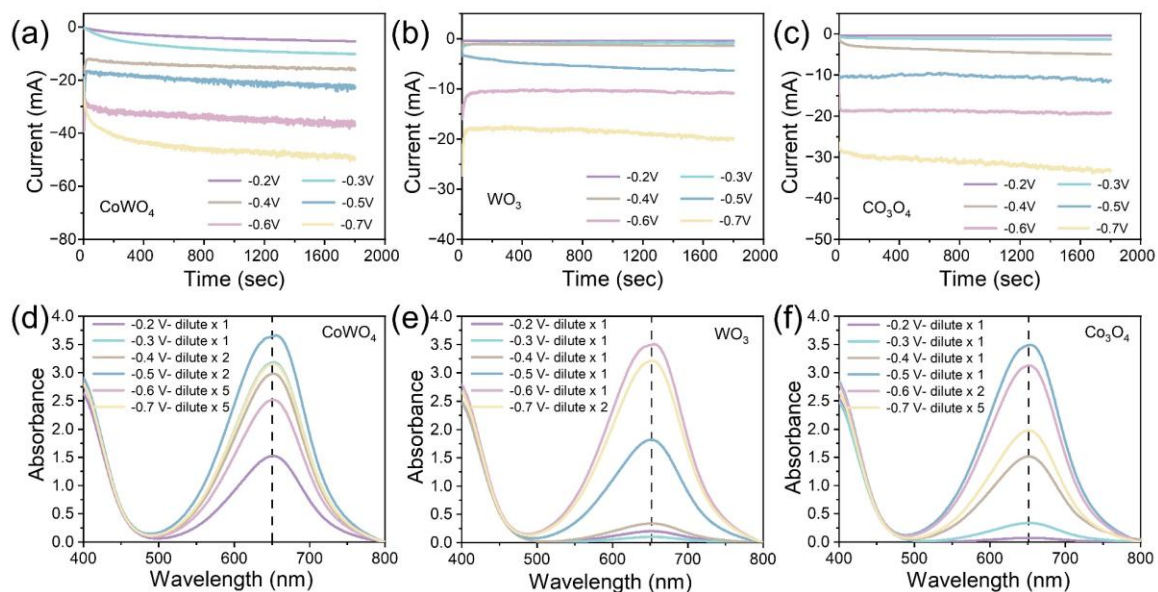


Figure S19 I-t curves of (a) CoWO₄, (b) WO₃, and (c) Co₃O₄ electrolytes in 1M NaOH and 0.1 M NaNO₃ at different potentials for 30 minutes of electrolysis; UV-vis absorption spectra for NH₃ determination of (d) CoWO₄, (e) WO₃, and (f) Co₃O₄ at different potentials.

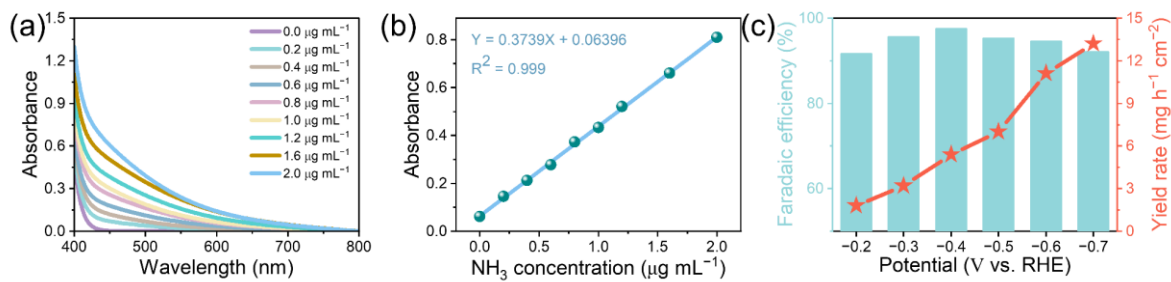


Figure S20 (a) UV-vis absorption spectra of Nessler's reagent assays for the standard NH_3 solutions with different concentrations; (b) corresponding calibration curve for the NH_3 assay; (c) NH_3 yield rates and FEs.

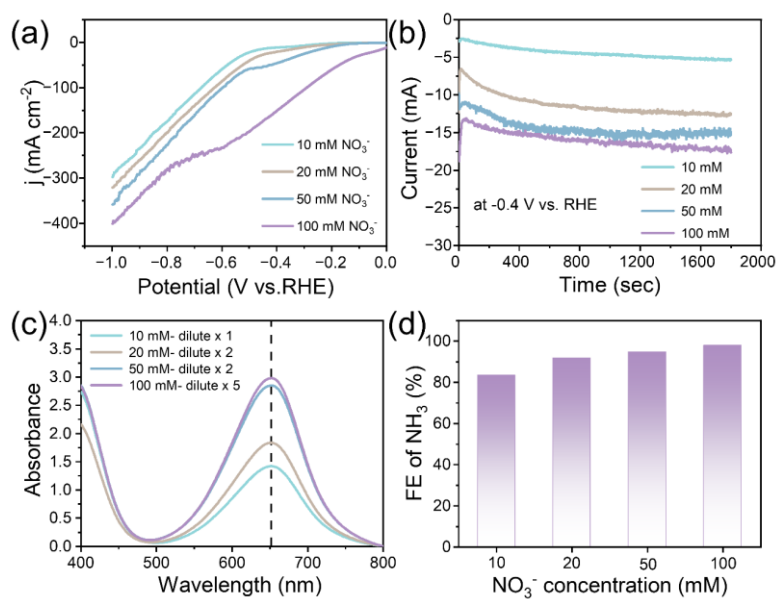


Figure S21 Performance of NO₃RR for CoWO₄ at different NO₃⁻ concentrations (100 mM, 50 mM, 20 mM, and 10 mM): (a) LSV curve; (b) chronoamperometric curves; (c) UV absorption spectra of corresponding NH₃ assay; (d) The FEs comparison of NH₃ production in different NO₃⁻ concentration electrolyte at -0.4 V.

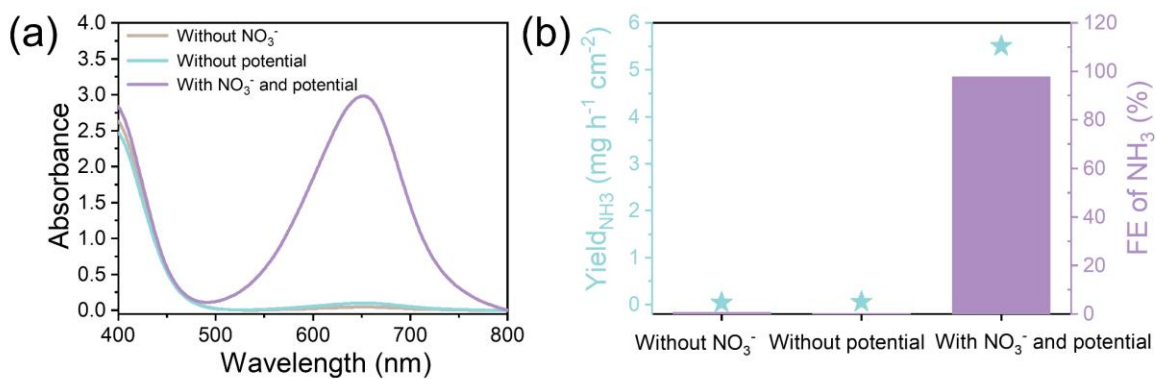


Figure S22 (a) UV absorption spectra of NH_3 assay for CoWO_4 catalyst under different conditions (presence and absence of NO_3^- in 1M NaOH electrolyte, and with and without voltage); (b) Yield and FE of NH_3 generation under different conditions.

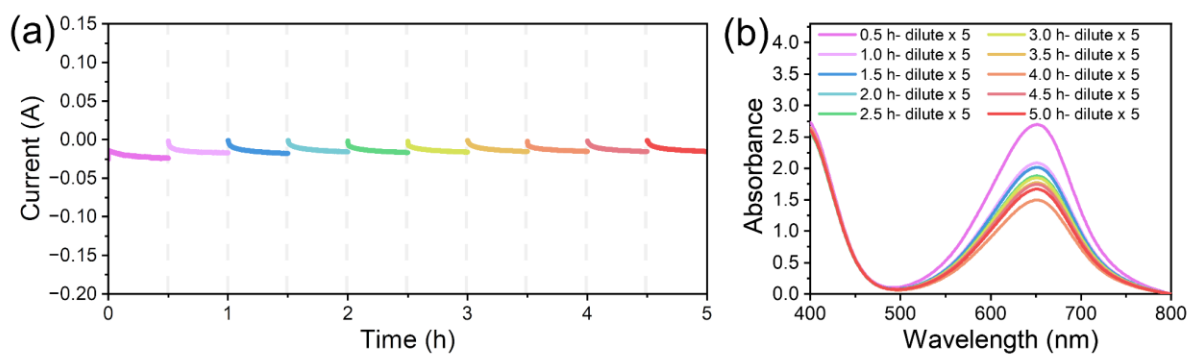


Figure S23 (a) I-t curve during cycling stability test of CoWO_4 at -0.4 V; (b) UV absorption spectrum of corresponding NH_3 measurement during cycling stability test.

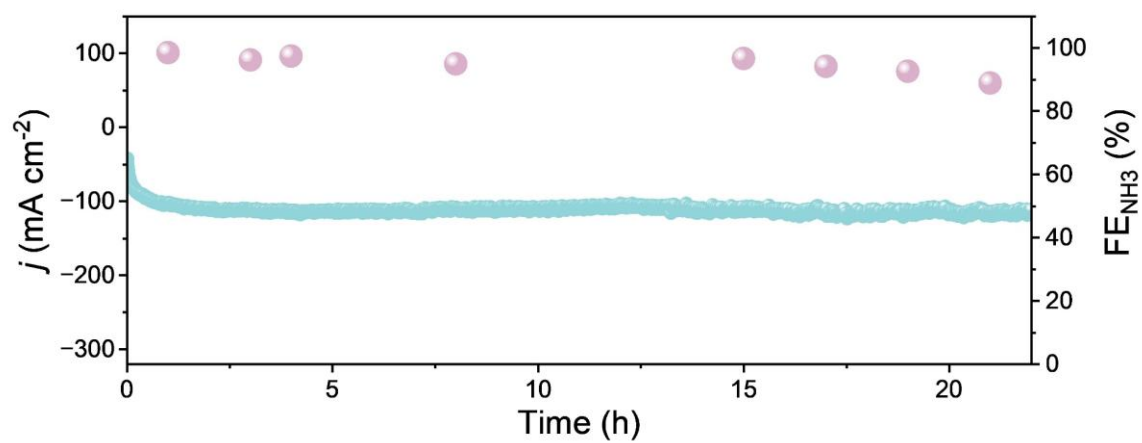


Figure S24 I-t curve and corresponding FE_{NH_3} during continuous long-term electrolysis test.

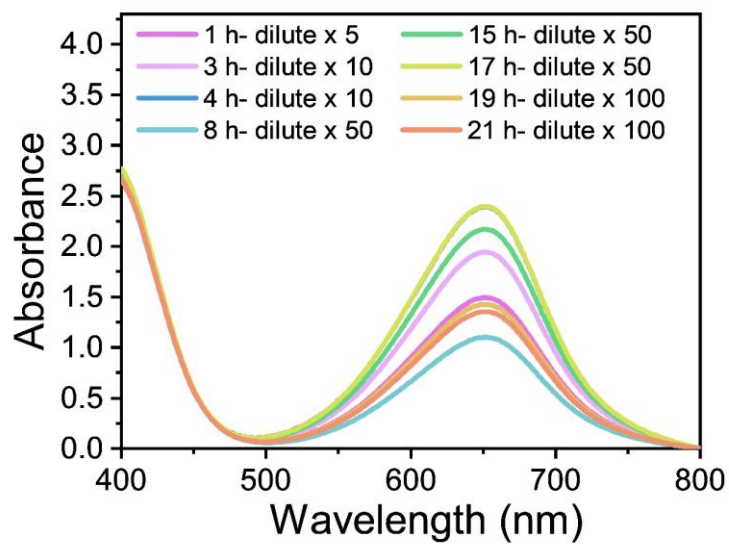


Figure S25 UV absorption spectrum of NH₃ measurement during continuous long-term electrolysis test.

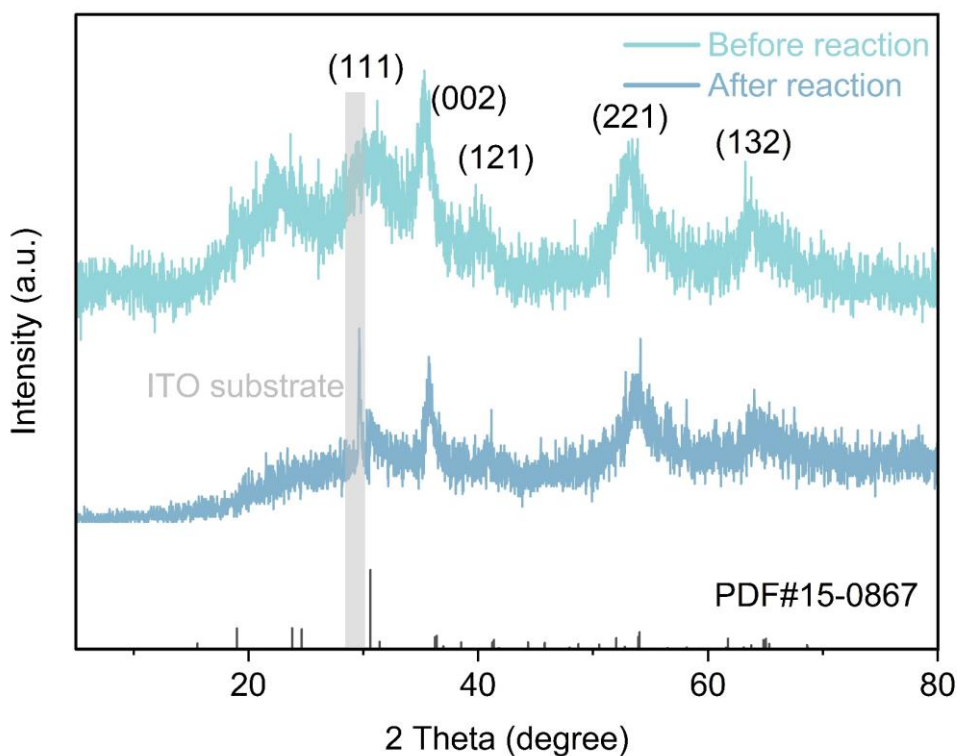


Figure S26 XRD patterns of CoWO_4 catalyst before and after electrochemical reaction.

During the XRD inspection process, the peaks of the catalyst material tend to be covered by the peaks of the carbon paper due to the use of carbon paper as a carrier to load the catalyst. In order to better show the difference before and after the electrochemical reaction, ITO glass was chosen as the substrate for the loaded catalyst.

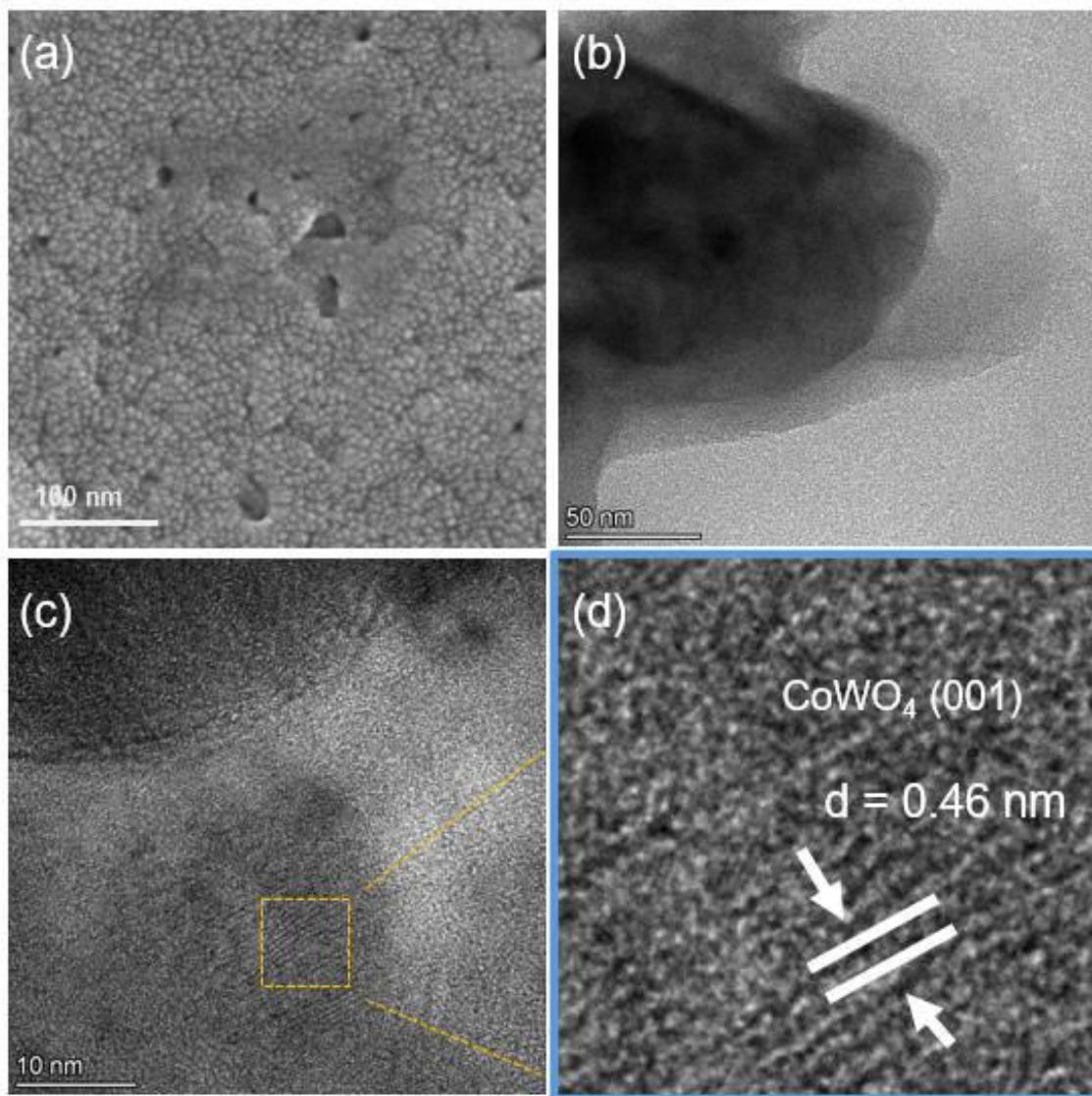


Figure S27 The structural characterizations of CoWO₄ after reduction. (a) SEM image; (b) TEM image; (c) HR-TEM image and (d) enlarged HR-TEM image.

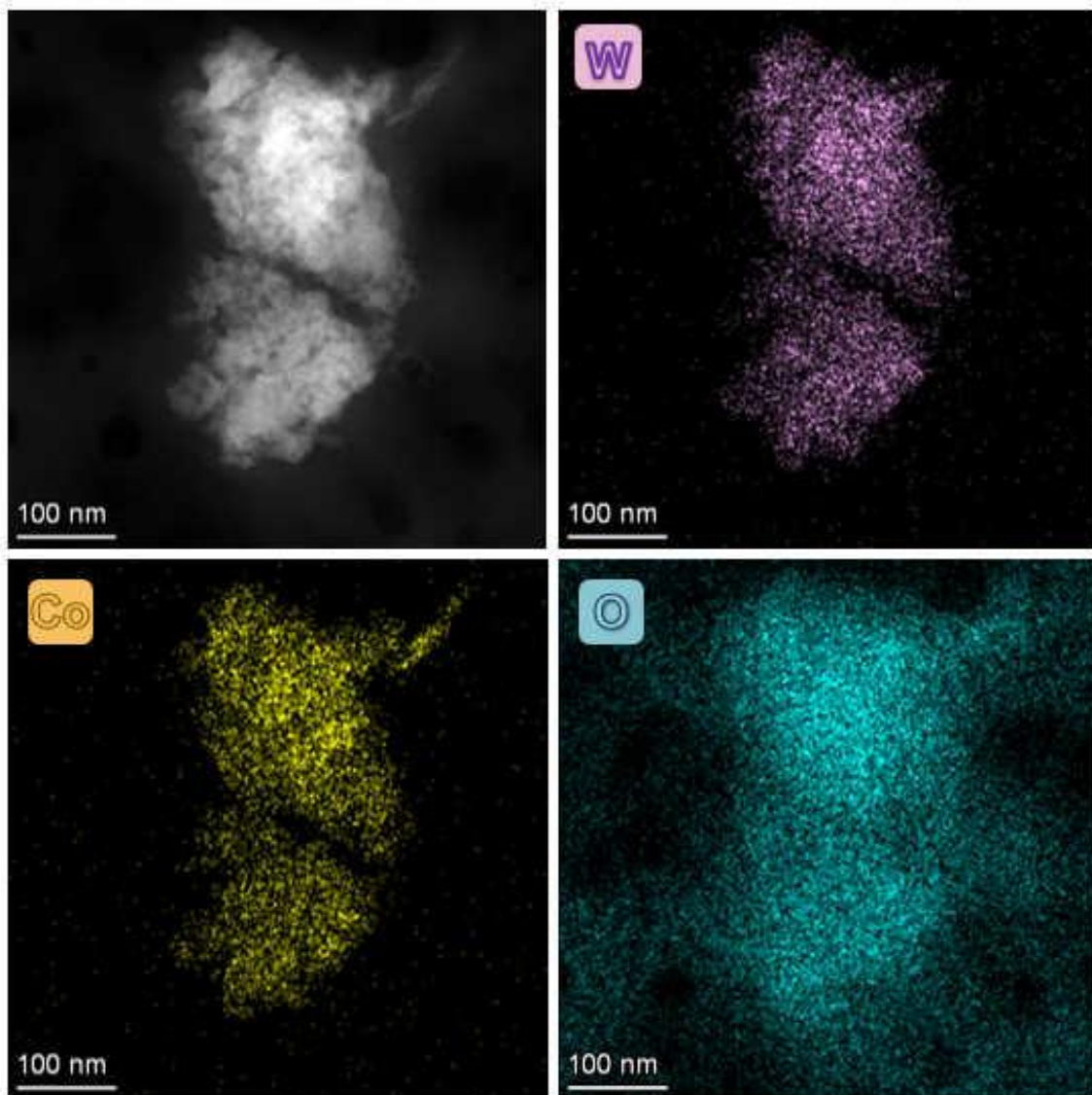


Figure S28 HAADF-STEM image of CoWO_4 after reduction and corresponding EDS elemental maps of W, Co, and O.

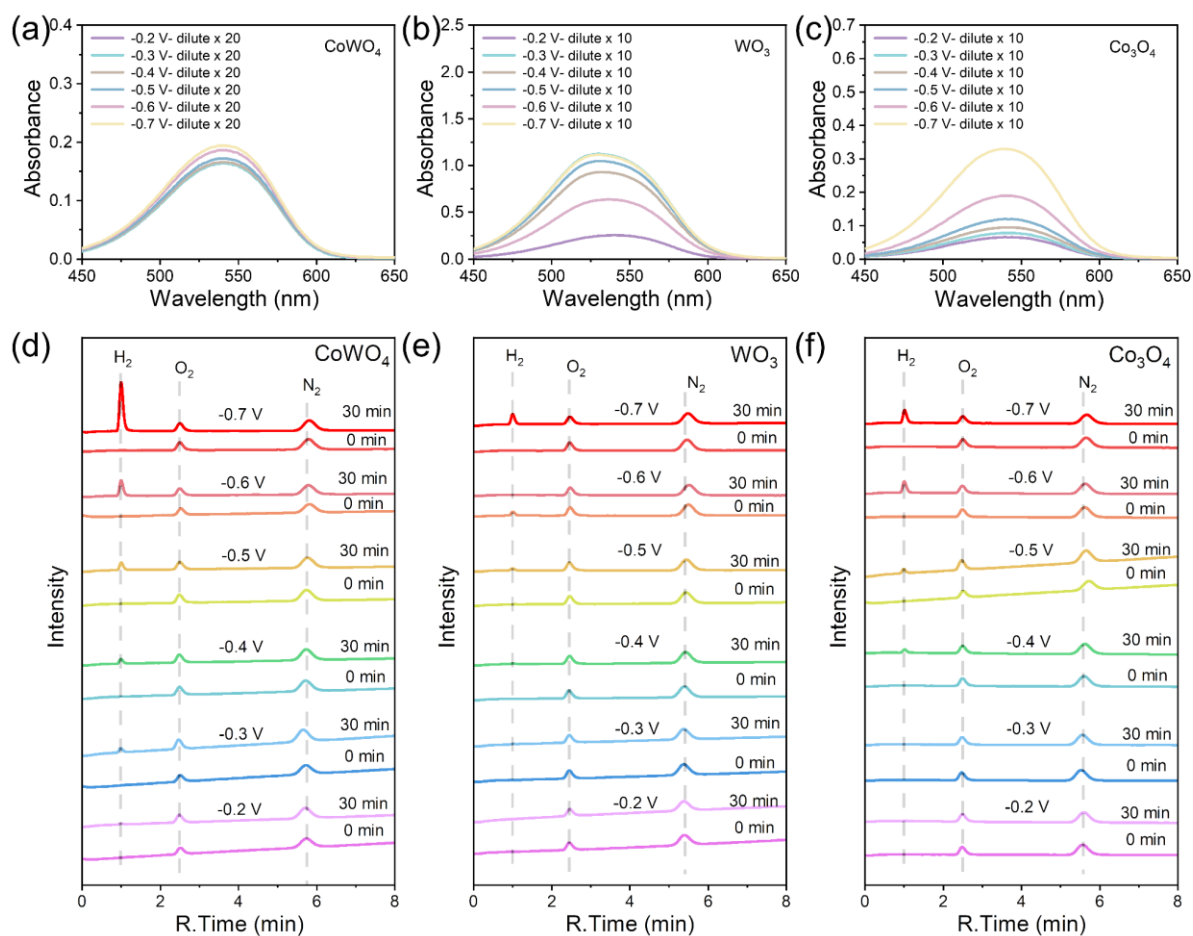


Figure S29 Measurement of side-products during the NO₃RR electrolysis. (a-c) UV-vis absorption spectra for NO₂⁻ determination of (a) CoWO₄, (b) WO₃, and (c) Co₃O₄ at different potentials; (d-f) Gas chromatography curves of H₂ and N₂ detected by GC during the electrochemical NO₃RR process of (d) CoWO₄, (e) WO₃, and (f) Co₃O₄ at different potentials.

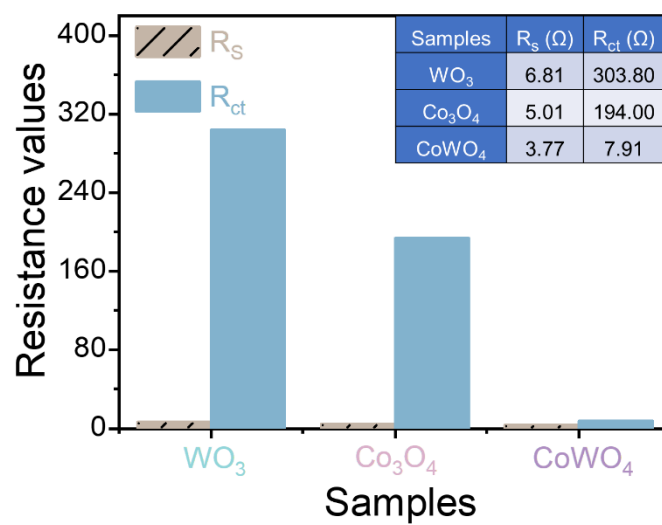


Figure S30 Comparison of R_s and R_{ct} (The inset shows the specific resistance values of R_s and R_{ct}).

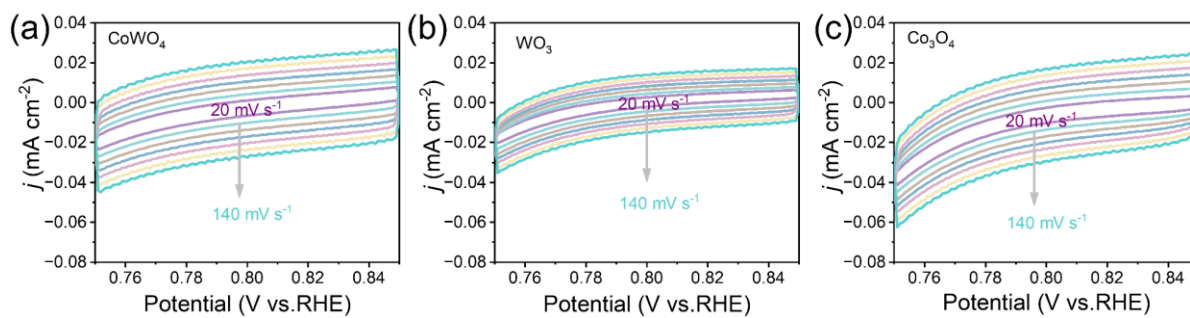


Figure S31 Cyclic voltammetry (CV) curves with different scanning rates for (a) CoWO₄, (b) WO₃, and (c) Co₃O₄.

Supplementary Table

Table S1 Comparison of NO₃RR performances for recently reported W-based and Mo-based electrocatalysts.

Catalysts	Electrolyte (NO ₃ ⁻ concentration)	FE (Potential, V vs. RHE)	J _{NH₃} (mA /cm ²)	NH ₃ yield (mg/cm ² /h)	Ref.
CoWO ₄	1.0 M NaOH (100 mM)	97.8% (-0.4 V)	148.10	5.5	This work
WSe ₂	0.5 M Na ₂ SO ₄ (100 mM)	92.7% (-0.8 V)	31.05	2.42	11
Co ₂ Mo ₆ S ₈	0.17 M Na ₂ SO ₄ (100 mM)	97.1% (-0.4 V)	4.95	0.023	12
WN/WO ₃	1.0 M NaOH (100 mM)	88.9% (-0.7 V)	113.24	8.4	13
V _{Co} - Co ₃ O ₄ /CC	0.1 M NaOH (100 mM)	97.2% (-0.4 V)	55.17	8.797	14
PdW	0.5 M Na ₂ SO ₄ (100 mM)	70.8% (-0.7 V)	14.16	2.3	15
Co ₁ -P/NPG	0.5 M K ₂ SO ₄ (100 mM)	93.8% (-0.7 V)	12.3	0.86	16
Mo/H-CuW	0.5 M Na ₂ SO ₄ (100 mM)	94.6% (-0.7 V)	19.04	1.46	17
P-CoMoO ₄	0.5 M Na ₂ SO ₄ (100 mM)	96.7% (-0.5 V)	19.3	1.056	18

References

- 1 G. Kresse and J. Furthmüller, *Phys. Rev. B*, 1996, 54, 11169-11186.
- 2 J. P. Perdew, K. Burke and M. Ernzerhof, *Phys. Rev. Lett.*, 1996, 77, 3865-3868.
- 3 G. Kresse and D. Joubert, *Phys. Rev. B*, 1999, 59, 1758-1775.
- 4 S. Grimme, J. Antony, S. Ehrlich and H. Krieg, *J. Chem. Phys.*, 2010, 132.
- 5 J. K. Nørskov, J. Rossmeisl, A. Logadottir, L. Lindqvist, J. R. Kitchin, T. Bligaard and H. Jónsson, *J. Phys. Chem. B*, 2004, 108, 17886-17892.
- 6 Z. Shu, H. Chen, X. Liu, H. Jia, H. Yan and Y. Cai, *Adv. Funct. Mater.*, 2023, 33, 2301493.
- 7 Y. L. Oliveira, A. F. Gouveia, M. J. S. Costa, F. H. P. Lopes, J. C. Sczancoski, E. Longo, G. E. Luz. Jr, R. S. Santos and L. S. Cavalcante, *Materials Science for Energy Technologies*, 2022, 5, 125-144.
- 8 Y. Sun, S. Liu, N. Huang, X. Wang, J. Liu, J. Bi, J. Zhang, L. Guo and X. Sun, *J. Power Sources*, 2022, 545, 231911.
- 9 S. S. Patil, U. M. Chougale, R. K. Kambale and V. J. Fulari, *Journal of Energy Storage*, 2023, 67, 107517.
- 10 S. Sagadevan, J. Podder and I. Das, *J. Mater. Sci.: Mater. Electron.*, 2016, 27, 9885-9890.
- 11 P. Shen, G. Wang, K. Chen, J. Kang, D. Ma and K. Chu, *J. Colloid Interface Sci.*, 2023, 629, 563-570.
- 12 B. Li, F. Xia, Y. Liu, H. Tan, S. Gao, J. Kaelin, Y. Liu, K. Lu, T. J. Marks and Y. Cheng, *Nano Lett.*, 2023, 23, 1459-1466.
- 13 Z. Huang, B. Yang, Y. Zhou, W. Luo, G. Chen, M. Liu, X. Liu, R. Ma and N. Zhang, *ACS Nano*, 2023, 17, 25091-25100.
- 14 Z. Deng, C. Ma, Z. Li, Y. Luo, L. Zhang, S. Sun, Q. Liu, J. Du, Q. Lu, B. Zheng and X. Sun, *ACS Appl. Mater. Interfaces*, 2022, 14, 46595-46602.
- 15 X. Li, G. Zhang, N. Zhang, Y. Luo, P. Shen, X. Li and K. Chu, *New J. Chem.*, 2022, 46, 14724-14730.
- 16 J. Ni, J. Yan, F. Li, H. Qi, Q. Xu, C. Su, L. Sun, H. Sun, J. Ding and B. Liu, *Adv. Energy Mater.*, 2024, 14, 2400065.
- 17 D. Chen, S. Zhang, X. Bu, R. Zhang, Q. Quan, Z. Lai, W. Wang, Y. Meng, D. Yin, S. Yip, C. Liu, C. Zhi and J. C. Ho, *Nano Energy*, 2022, 98, 107338.
- 18 Y. You, H. Chen, J. Guo, Z. Feng, J. Zhan, F. Yu and L.-H. Zhang, *Appl. Catal. B: Environ.*, 2025, 363, 124837.